ACS APPLIED NANO MATERIALS

www.acsanm.org

Article

Nearly Real-Time Monitoring of Magnetic Nanoparticle-Mediated Photothermal Therapy by MRI-Based Proton Resonance Frequency Thermometry

Published as part of ACS Applied Nano Materials special issue "Biomedical Imaging Contrast Agents".

Rafael Freire Krause, Maria de Paula Pereira, Carlos Eduardo Ribeiro, João Victor Ribeiro Rocha, Marcus Vinícius-Araújo, Lucas Ferreira Martins, Juracy Leandro Santos Junior, Clever Gomes Cardoso, Marcilia Viana Pavam, Luciano Morais Lião, and Andris Figueiroa Bakuzis*

Cite This: *ACS Appl. Nano Mater.* 2025, 8, 21774−21787

Read Online

ACCESS | Metrics & More | Article Recommendations | Supporting Information

ABSTRACT: Iron oxide-based nanoparticles (NPs) have been used in the clinic for decades, making them strategic for clinical applications. Monitoring magnetic NP-mediated photothermal therapy (PTT) with MRI thermometry is challenging due to susceptibility effects, which might explain the limited progress in clinical translation. Here, we explore Mn-ferrite NPs for PTT and demonstrate ex vivo and in vivo noninvasive MRI thermometry using the proton resonance frequency shift (PRF) method. We observed a high external photothermal efficiency at 808 nm, 0.8 $g \cdot L^{-1} \cdot cm^{-1}$. Temperature-dependent NMR spectroscopy of the B16F10 tumor revealed a PRF coefficient of -0.0091 ppm·°C^{-1}. The image artifact for this NP was quantified, which resulted in a radius increase distortion of 0.75 mm using 1 $mg \cdot mL^{-1}$ of NP. PRF thermometry was effectively monitored at the boundary regions of NP locations that guided the therapeutic procedure. In vivo experiments at a power density of 1.25 $W \cdot cm^{-2}$ using the melanoma model confirmed MRI-PRF thermometry and demonstrated that NP-mediated PTT improves the distribution of thermal doses within the tumor compared to laser therapy alone. Challenges for ablation application are discussed, suggesting opportunities for magnetic NP design. These results may pave the way for the clinical translation of PTT with magnetic NPs.

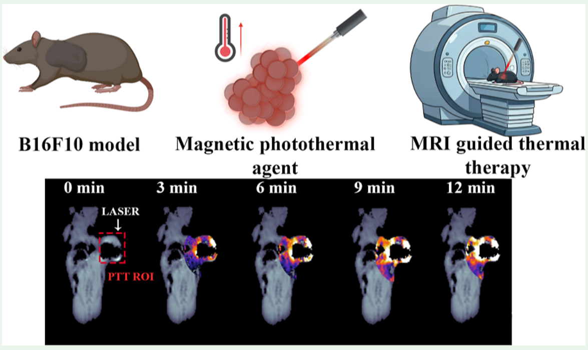

KEYWORDS: *nanomedicine, thermal therapy, thermometry, cancer, magnetic resonance*

1. INTRODUCTION

Thermal therapy is commonly used in the clinic to treat cancer, but it might benefit other diseases.[1−7] Examples of heating methods include high-intensity focused ultrasound (HIFU), laser interstitial thermal therapy, magnetic nanoparticle hyperthermia (MNH), and nanoparticle-mediated photothermal therapy (NP-PTT), among others.[3,8−11] The localized temperature increase enhances blood perfusion and cell membrane diffusion, contributing to excellent clinical outcomes when combined with radiotherapy and chemotherapy.[2,12] In addition, heat-triggered drug release in situ has been demonstrated.[12,13] Perhaps the most exciting development lies in the potential application of thermal therapy for immunotherapy, since heat can activate innate and adaptive immune cell responses.[1]

The major challenge is real-time temperature monitoring during therapeutic procedures. Different thermometry methods were proposed,[14−16] but the gold standard technology remains MRI thermometry, particularly the proton resonance frequency shift (PRF) method.[17−21] This approach is currently used to monitor brain tumor thermal therapy.[7,9,10] However, an interesting advance of this strategy is the application of nanoparticle-mediated PTT,[22] where photoconversion agents generate heat in a well-defined region of interest, minimizing nonspecific heat generation.

The concept of monitoring PTT with MRI is not new. Silica−gold nanoshells (SiO_2@Au core@shell NPs) were among the first nanostructures used to monitor PTT through PRF thermometry.[23] This idea was recently explored in a clinical study involving patients with early stage prostate cancer, who reported a high tumor ablation rate with negligible

Received: August 5, 2025
Revised: October 23, 2025
Accepted: October 24, 2025
Published: October 31, 2025

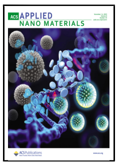

https://doi.org/10.1021/acsanm.5c03647

post-treatment morbidity, no increase in incontinence, and preserved sexual function.[4] The findings highlighted the need to localize NP before PTT, prompting the same group to incorporate ultrasmall Gd-oxide NP (an MRI contrast agent) into mesoporous silica.[24] This approach may be useful for determining the intratumoral biodistribution of photoconversion agents and for improving treatment planning. Recently, Gd-doped fluoride ($NaBiF_4$:Gd) NPs and Pluronic-Gd-DTPA NPs have also been proposed for MRI-guided PTT and HIFU, respectively.[8,25] Interestingly, there are concerns about Gd-based materials due to their association with nephrogenic systemic fibrosis in patients with chronic kidney disease, leading to investigations of alternative strategies, such as Mn-based contrast agents.[26] Furthermore, most PTT-based nanomaterials studied to date have not been approved for clinical use.[27,28] The selection of materials already approved for clinical applications that can generate PTT-induced heat might represent a promising strategy.

Iron oxide-based NPs are used in the clinic for decades, primarily for applications such as anemia treatment, MRI contrast agents, and magnetic hyperthermia.[27] In particular, Feraheme, an iron deficiency therapeutic agent, has demonstrated interesting immunotherapeutic properties in murine models, slowing tumor growth and reducing metastatic focus by promoting macrophage polarization to the M1 state.[29] These NPs can biodegrade and release metallic ions (e.g., Fe, Mn, Zn), which play a significant role in immunological processes.[30] The combination of NPs with thermal therapy is expected to further enhance immunotherapy.[31−33] For example, PTT-induced immunogenic cell death has been reported using Prussian blue NPs and Mn-doped iron oxide NPs.[32,34] In addition, evidence of heat-induced abscopal effects has also been reported.[35,36]

In this study, Mn-ferrite NPs were selected due to their diverse biomedical applications, including vaccine adjuvants, magnetic hyperthermia and PTT agents, magnetic tracers, MRI contrast agents, and immunotherapy.[32,37−44] Previous in vivo studies confirmed the safety of these theranostic NPs within the concentration range tested.[37,39−43,45−49] However, combining magnetic NPs for MRI-guided thermal therapy presents significant challenges. High magnetic NPs concentrations can affect spatial reconstruction and phase coherence, distorting the MRI image. To our knowledge, no prior study has properly quantified this effect. This limitation may explain why iron oxide NPs have seen limited use as contrast agents in a real clinical scenario, where T_1 contrast agents are generally preferred. More importantly, susceptibility effects might affect the application of magnetic NPs with PRF-MRI thermometry. This belief likely impacted progress in the field with this type of nanomaterial.

Here, we show that, although the exact location of the NPs cannot be monitored because of rapid relaxation effects, the boundary regions can still be visualized. This enables clinicians to plan and control the therapeutic procedure, particularly in ablation applications, where accurate monitoring of treatment boundaries is crucial for therapeutic success. Iron oxide-based NPs are excellent photoconversion agents that require a lower amount of NPs, which might minimize the susceptibility effects on the PRF method. An experiment was designed to quantify the image artifact distortion, which results in apparent larger boundaries depending on NP characteristics. We explore the role of Mn-doped iron oxide NPs for photothermal therapy and demonstrate ex vivo and in vivo the possibility of monitoring the thermal dose during PTT with the PRF magnetic resonance thermometry method. This breakthrough might accelerate the clinical translation of PTT, as iron oxide-based NPs can also trigger cancer immunotherapy, affecting patient survival and quality of life. The challenges for ablation application are also discussed, suggesting new opportunities for magnetic NP design.

2. MATERIALS AND METHODS

2.1. Chemicals. Manganese(II) chloride tetrahydrate ($MnCl_2\cdot 4H_2O$), iron(III) chloride hexahydrate ($FeCl_3\cdot 6H_2O$), methylamine solution 40 wt % in H_2O (CH_3NH_2), and sodium citrate tribasic dihydrate ($Na_3C_6H_5O_7\cdot 2H_2O$) were purchased from Sigma-Aldrich (St. Louis, Missouri, USA).

2.2. Magnetic Nanoparticle Synthesis. The magnetic NPs were synthesized using the hydrothermal method. The precursor ions (Mn^{2+} and Fe^{3+}) were obtained from 1 M solutions of manganese chloride tetrahydrate ($MnCl_2\cdot 4H_2O$), and iron chloride hexahydrate ($FeCl_3\cdot 6H_2O$). Methylamine (CH_3NH_2) was used as the precipitating agent, with 10 mL of CH_3NH_2 diluted in 40 mL of Milli-Q water. First, 10 mL of the $FeCl_3\cdot 6H_2O$ solution and 5 mL of $MnCl_2\cdot 4H_2O$ solutions, were mixed in a Teflon recipient. The CH_3NH_2 solution was then added to the mixture, forming a dark precipitate. The resulting solution was stirred for 10 min. Subsequently, the Teflon recipient holding the mixture was placed in a stainless steel autoclave and heated to 160 °C for 4 h. After the reaction time, the NPs were magnetically separated and washed 3 times with Milli-Q water. Then, the NPs were prepared for citrate coating to ensure their colloidal stability at physiological pH. For coating, NPs were diluted in Milli-Q water and sodium citrate ($Na_3C_6H_5O_7$) was added in a ratio of 1 mol of citrate for every 10 mol of iron in the sample. The resulting solution was heated to 80 °C and stirred for 10 min. After being cooled to room temperature, the NPs were magnetically separated again and the supernatant was discarded. The sample was washed 3 times with acetone and, after complete evaporation of the acetone, the NPs were suspended in Milli-Q water, completing the preparation of the magnetic fluid.

2.3. Morphology, Crystallinity, Size, Surface Charge, Optical and Magnetic Properties of NPs. Morphology was assessed by transmission electron microscopy (TEM) using a JEOL JEM-2100 microscopy (Tokyo, Japan). The magnetic fluid was diluted in water and a droplet was deposited on the carbon film of a TEM copper grid. SAED images were captured with a 40 cm camera length and analyzed using GATAN's Digital Micrograph software, including FFT, IFFT, and HRTEM techniques. NP size analysis, assuming spherical symmetry, was performed with ImageJ software. A log−normal distribution was applied to the diameter histogram, providing the size dispersity and the median diameter. XRD measurements of powder sample of $MnFe_2O_4$-based NPs were performed using a Bruker Discover D8 X-ray diffractometer with Cu Kα radiation (wavelength = 0.15 nm). Zeta-potential measurements were performed using a Zetasizer Nano ZS90 (Malvern Panalytical, Westborough, United States). Room-temperature magnetization data was obtained using a VSM model EV9 from ADE Magnetics. The absorbance data were acquired using a Kasvi K37-UVVIS spectrophotometer. AC susceptometry were measured using a DynoMag AC susceptometer (RISE, Boras, Sweden).

2.4. MRI Characterization. MRI measurements were performed at 20 °C with the 1.0 T M7 Compact MRI system from Aspect Imaging. The $MnFe_2O_4$ sample were diluted in 14 mL of water from their original batch to obtain concentrations in the range of 0.06 mM to 0.24 mM of [Mn] + [Fe]. The determination of T_1 used an snapshot flash sequence. The sequence used a short echo time (TE = 1.9 ms) to reduce the influence of T_2 on the intensity of the MRI signal. Inversion times ranged from 25 to 800 ms with repetition time TR = 4500 ms, flip angle FA = 6° and voxel dimension of $(0.75 \times 0.75 \times 1)$ mm^3. T_2 is obtained using a spin echo pulse sequence with a high repetition time (TR = 4000 ms), to minimize the effect of longitudinal relaxation T_1 on the signal. The same voxel dimension was used. Echo times ranged from 7.5 to 25 ms. The same pulse sequences were used for the contrast agent ProHance with slight variations in inversion and echo times. The samples were diluted to concentrations in the range of 0.25 to 0.55 mM of [Gd] for the determination of T_1 and 5 to 20 mM for the determination of T_2 to produce a significant decay. The signal intensity profiles of the samples are shown in Supporting Information, Figure S1.

2.5. NMR Spectroscopy. The ^{1}H HR-MAS NMR experiments were acquired on a Bruker Avance III 500 spectrometer (Bruker, Rheinstetten, Germany) operating at 11.75 T (500 MHz for ^{1}H), fitted with a 4 mm four radiofrequency channels (^{1}H, ^{2}H, ^{13}C and ^{15}N) HR-MAS probe with a magic angle gradient. The samples were spun at 5 kHz. For data acquisition, 0.12% (m/m) of a solution of DMSO-d_6 and trimethylsilyl propionate-d_4 (TMSP-2,2,3,3-d_4) was used. The amounts of sample and solvent used in each experiment are described in Supporting Information, Table S1.

2.6. Photothermal Conversion Efficiency Measurement. The photothermal properties of the $MnFe_2O_4$-based NPs were investigated using a laser with a 808 nm wavelength, model Laser iZi 808, bought from LASERline (Sao Paulo, Brazil). The temperature was monitored with an infrared thermal camera (FLIR, SC620 model, Wilsonville, United States). A region of interest (ROI) centered on the laser spot was selected to report the mean temperature during PTT.

The photothermal conversion efficiency (PCE) was estimated using the droplet method and calculated using the equation

$$\mathrm{PCE} = \frac{hS(T_{\max} - T_0) - Q_0}{P(1 - 10^{-A(\omega)})} \tag{1}$$

where h is the heat transfer coefficient, S is the surface area of the sample, $T_{\max}$ is the maximum temperature reached under laser irradiation, T_0 is the room temperature, P is the laser power and $A(\omega)$ is the absorbance of the sample at the laser wavelength. The parameter Q_0 is the heat absorbed by the liquid carrier and sample holder and is determined experimentally. PCE was calculated using Roper's method,[50] with τ estimated from the PTT cooling curve immediately after the laser was turned off.[32] The external photothermal conversion efficiency (ePCE) was obtained according to Paściak et al.,[51] which is defined as ePCE = a_λPCE. In this equation, a_λ is given by $a_\lambda = \frac{A_\lambda}{cL}$, where A_λ represents the absorbance at a specific wavelength, c is the mass concentration (mg·mL^{-1}), and L is the optical path (cm).[51] The absorbance profile of the sample are shown in Supporting Information, Figure S2.

2.7. PRF Implementation. To implement PRF thermometry in our preclinical MRI system, we addressed two challenges: irradiating the sample within the MRI equipment, and writing a script *python* to process raw MRI data from consecutive spoiled GRE pulses.

The near-infrared homemade fiber optic laser system was developed using a commercial diode laser bought from Zhuhai AIKE Photonics Technology, China, that had a SMA-905 fiber connector. The 808 nm laser diode has core diameter of 400 μm and a maximum power of 15 W. The system has a current controller board that tunes the laser power. On the front panel of the system is a display that shows the voltage and current supplied to the diode, an on/off key and a button to adjust the current supplied to the laser. The fiber optical cable was bought from Thorlabs (New Jersey, United States) and is coupled to the laser through the SMA905 connector. Fiber optic cables have a length of 2 m and a diameter of 200 μm and guide the laser beam to the sample inside the MRI equipment while the script calculates phase changes at each voxel to determine temperature changes.

MRI images contain signal intensity (influenced by spin density, relaxation time, and pulse sequence parameters) and phase (ϕ), defined as $\phi = \omega$TE, where TE is the spin echo time. The resonance field frequency ω depends on the MRI magnetic field (B_0), chemical shift (σ), susceptibility (χ), and field inhomogeneity (δB) as

$$\omega = \gamma[B_0(1 - \sigma(T) + c\chi(T)) + \delta B] \tag{2}$$

where γ is the proton gyromagnetic ratio. For low NP concentrations, the susceptibility term is negligible, and the PRF temperature dependence is modeled by $\sigma = \alpha T$, with α as the PRF coefficient. The temperature change is determined by the following.

$$\Delta T = -\frac{\Delta\phi}{\gamma B_0 \alpha \mathrm{TE}} \tag{3}$$

This analysis enables real-time temperature mapping during PTT. The GRE sequence used for the MRI thermometry consisted in a single slice (0.75 × 0.75 × 2) mm^3 spoiled GRE sequence with repetition time TR = 80 ms, echo time TE = 4 ms and flip angle FA = 15°, acquisition time was 12 s.

2.8. Ex Vivo Experiments. Small pieces of pork loin were perforated with a glass capillary tube holding 50 μL of magnetic NP at multiple concentrations. GRE and SE sequences were performed to evaluate the capillary tube width in the central slice of the sample with varying concentrations of NPs. The outer diameter of the tube was measured at 1.50 mm with a caliper.

For the PTT trials, two samples were evaluated, one with 50 μL of magnetic NPs at 1 mg·mL^{-1}, and another with 50 μL of water. The initial temperature of the material was measured to be 21 °C. The PTT trials consisted of 3 min at constant temperature (laser off) to evaluate the mean deviation of the PRF data at constant temperature, followed by 10 min of irradiation at 2.5 W·cm^{-2} or 1.0 W·cm^{-2} (laser on) and 10 min of cooling (laser off). During the trial, a series of GRE sequences were acquired and used to perform MRI thermometry with a time resolution set to 12 s and an estimated temperature accuracy of 0.8 °C for the 1 T MRI system.

Additional PTT trials were conducted to compare MRI thermometry with surface temperature monitoring using an infrared thermal camera. The heating of one sample containing 10 μL of Mn-ferrite NPs at 10 mg·mL^{-1} was evaluated through measurements with the thermal camera and by MRI thermometry during irradiation at 1.25 W·cm^{-2}.

2.9. In Vivo Experiments. As a proof-of-concept experiment, female C57Bl/6 mice, 8 to 10 weeks old and with an average body weight between 20 and 30 g, were used for in vivo studies. The animal maintenance conditions and experimental procedures for the animal study, as well as general anesthesia (isoflurane) and euthanasia protocols, were reviewed and approved by the Ethics Committee for the Use of Animals (CEUA) of the Federal University of Goias under protocol 109/22. Cells from the B16F10 murine melanoma lineage were obtained from the Rio de Janeiro Cell Bank (BCRJ, Rio de Janeiro, Brazil). Solid tumors were induced in the dorsal region of the animals by inoculating, by subcutaneous injection, 50 μL of solution with 1 × 10^6 viable cells. Tumor volume measurements were performed with a digital caliper daily. Tumor volume was calculated as follows

$$V = \frac{Dd^2}{2} \tag{4}$$

where D is the long axis and d is the short axis of the solid tumor in mm.

Six animals were divided into two groups (control and NP) and used for the PTT study, while two additional animals were euthanized for PRF coefficient determination. Animals in the NP group received an intratumoral administration of 10 μL of Mn-ferrite NPs at 10 mg·mL^{-1}. Both control and NP group animals were evaluated using coronal and sagittal T_1W spin−echo pulse sequences with TR = 600 ms, TE = 10 ms, and a voxel dimension of (0.25 × 0.25 × 1.0) mm^3 to assess the tumor area. A series of spoiled GRE sequences were acquired to perform MRI thermometry during thermal therapy, which consisted of 10 min of irradiation at 1.25 W·cm^{-2} followed by an additional 5 min of cooling monitoring. All procedures were performed under general anesthesia.

2.10. Histopathology. A histopathological examination was performed on the spleen, kidneys, heart, lungs, liver, and tumor of both control and NP-injected groups using hematoxylin and eosin (HE) staining. The tissues were fixed in 4% paraformaldehyde in a 0.1

Scheme 1. Scheme of the Hydrothermal Synthesis of Mn-Ferrite NPs Surface-Coated with Citrate Molecules[a]

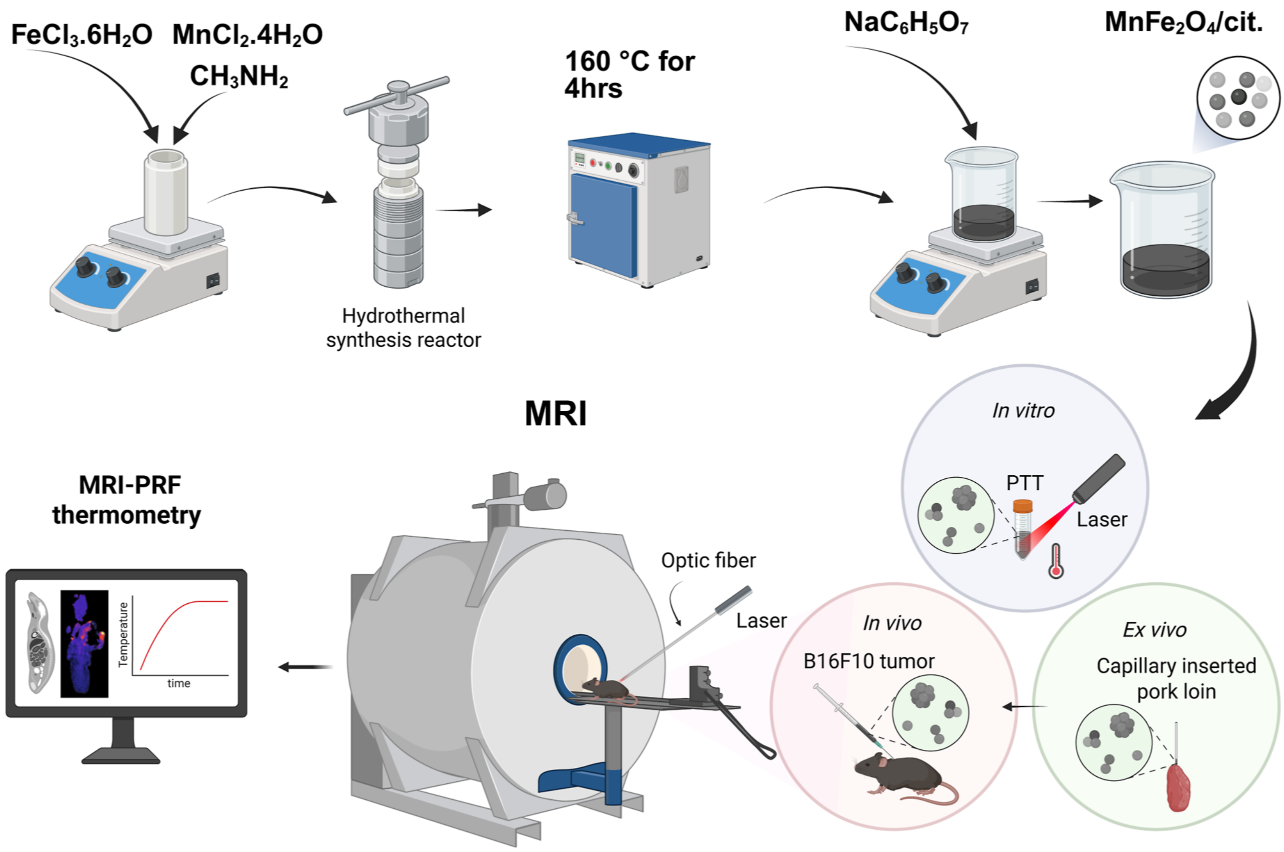

[a] The application of the nanomaterial for photothermal therapy was investigated in vitro, ex vivo, and in vivo using the B16F10 murine melanoma tumor model. Ex vivo and in vivo heat delivery studies during thermal therapy were monitored by the MRI proton resonance frequency shift method.

mol·L^{-1} phosphate buffer solution at pH 7.2 for 24 h. They were then dehydrated in a graded series of ethanol solutions (70%, 80%, 90%, and 100%), diaphonized in xylene, and embedded in histological paraffin paraplast. The blocks were sectioned into 5 μm-thick slices using a Leica RM2245 microtome and stained with HE. Additionally, 5 μm tumor sections from treated animals were stained with Perls' Prussian blue, consisting of a 10% hydrochloric acid and 5% potassium ferrocyanide solution for 30 min at room temperature, followed by counterstaining with safranin for 1 min. HE and Perls-stained sections were examined under a light microscope (Carl Zeiss Axiovert, Göttingen, Germany), and images were captured using Zeiss Microscopy Zen Software (×5, × 10, and × 20).

2.11. Statistical Analysis. The results were expressed as mean ± standard deviation from multiple experimental replicates. Nonparametric unpaired samples were compared using the Mann–Whitney test, while paired samples were compared using the Wilcoxon test, with statistical significance defined at $p < 0.05$. All analyses were performed using the *scipy* library in *python*.

3. RESULTS AND DISCUSSIONS

Scheme 1 shows the overall process of synthesizing Mn-ferrite NPs via a hydrothermal route and their surface functionalization with citrate molecules. The performance of these citrate-coated Mn-ferrite NPs was subsequently evaluated in photothermal therapy experiments conducted in vitro, ex vivo, and in vivo using the B16F10 murine melanoma model.

3.1. Characterization of the $MnFe_2O_4$ Nanoparticles. Figure 1a shows a TEM image of Mn-ferrite NPs coated with citrate ($MnFe_2O_4$/cit), revealing spherical morphology. The inset displays an HRTEM image and FFT analysis, identifying planes of the inverse spinel Mn ferrite ((311) and (220)) with a 0.14 nm interatomic distance. Figure 1b presents SAED patterns, indicating the polycrystalline nature of the NPs, with rings matching XRD data for planes (220) → 0.29 nm, (222) → 0.25 nm, (400) → 0.20 nm, (551) → 0.16 nm, and (440) → 0.14 nm. Figure 1c shows a size histogram, fitted with a log–normal function, yielding a mean NP diameter of 13 ± 3 nm. Figure 1d confirms the spinel cubic ferrite structure (space group $Fd\bar{3}m$, ICSD reference 00-010-0319). Figure 1e displays the magnetization curve, typical of a soft magnet, with a low coercive field (2.6 kA·m^{-1}) explained by larger particles in the blocked regime. The saturation magnetization of 301 kA·m^{-1} is lower than the bulk value, consistent with a core–shell model suggesting a weakly magnetic 1 nm shell that might be related to surface spin disorder.[52,53] The zeta potential of −32 mV confirms a successful citrate coating (see Supporting Information, Figure S3). The hydrodynamic size (D_H), measured by the imaginary AC susceptibility peak at 1 mg·mL^{-1} is 90.7 nm, suggesting a cluster of NPs, as shown in Figure 1f.

3.2. MRI Contrast Agent Properties. The MRI contrast properties of Mn-ferrite NPs were characterized using a preclinical 1 T MRI system (Aspect Imaging, model M7) and compared to the Gd-based contrast agent ProHance at 20 °C. Figure 1g shows the longitudinal relaxivity (r_1) of the NPs as 23 ± 1 mM^{-1} s^{-1}, compared to 6.10 ± 0.15 mM^{-1} s^{-1} for ProHance. For transverse relaxivity (r_2), Figure 1h shows 442 ± 4 mM^{-1} s^{-1} for the NPs versus 7.20 ± 0.66 mM^{-1} s^{-1} for

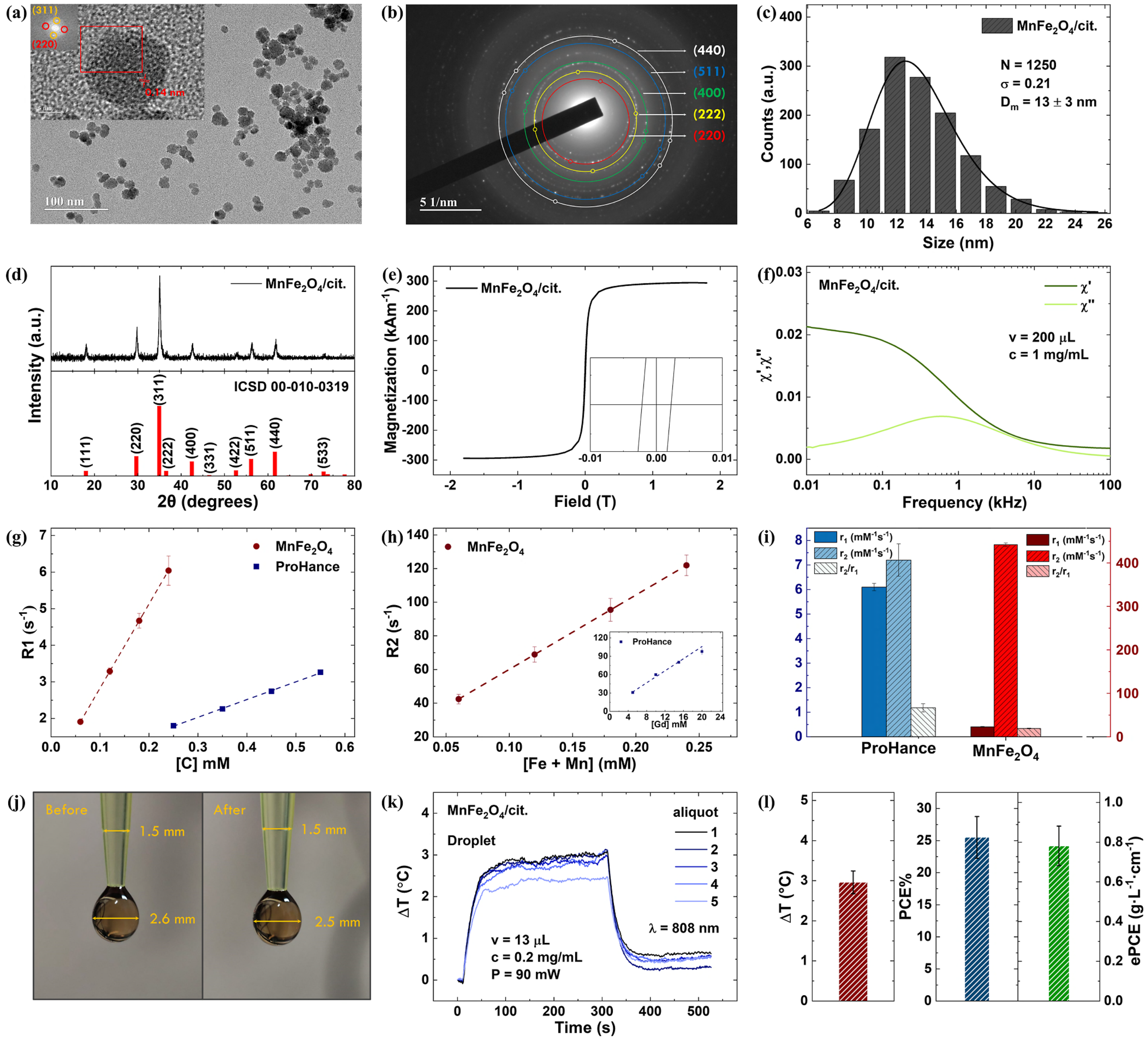

Figure 1. (a) TEM and HRTEM (inset) images for $MnFe_2O_4$ NPs. (b) SAED ring patterns of $MnFe_2O_4$ NPs confirming the spinel structure. (c) Log−normal size distribution of the NPs. (d) Powder X-ray diffraction data. (e) Room temperature magnetic hysteresis curve of the $MnFe_2O_4$ NPs. (f) AC susceptibility measurements of the Mn-ferrite based magnetic fluid. (g) Longitudinal relaxation (R1) of $MnFe_2O_4$ colloid and ProHance. (h) Transverse relaxation (R2) data of same samples. (i) r_1, r_2, and r_2/r_1 relaxivity values for $MnFe_2O_4$ colloid and ProHance. (j) Representative droplet image of $MnFe_2O_4$ colloid before and after PTT. (k) Temperature profile during the PTT study of distinct Mn-ferrite aliquots. (l) Temperature variation, PCE and ePCE values of $MnFe_2O_4$ NPs.

ProHance. The r_2/r_1 ratio, shown in Figure 1i, was 19.21 ± 0.85 for the NPs and 1.18 ± 0.17 for ProHance, confirming that ProHance is a T_1 contrast agent, while Mn-ferrite NPs act as T_2 agents. Mn-ferrite NPs are among the best T_2 contrast agents,[54] but reducing their size may allow them to be tuned to T_1 agents.[55]

3.3. Mn-Ferrite Nanoparticles Show Great Photothermal Performance. The photothermal performance was evaluated using the droplet method.[51] Figure 1j shows a representative droplet image before and after PTT for $MnFe_2O_4$ NPs. A slight volume change was observed, but this did not affect the determination of PTT efficiency. Aliquots at a concentration of 0.2 mg·mL^{-1} (to prevent evaporation) with 13 μL droplet volume were tested at 90 mW at 808 nm. Figure 1k shows the temperature variation of the aliquots, with a mean temperature increase of 3.0 ± 0.3 °C. The photothermal conversion efficiency (PCE) was 26%, and the external photothermal conversion efficiency (ePCE) was 0.8 ± 0.1 g·L^{-1}·cm^{-1} (Figure 1l). The ePCE for Mn-ferrite NPs is approximately 10 times higher than previously reported for maghemite NPs,[51] highlighting their excellent PTT performance in the near-infrared region.

3.4. PRF Coefficient for the B16F10 Tumor Model. Murine B16F10 melanoma tumors were induced in the dorsal region of female C57Bl/6 mice by subcutaneous injection of viable cells. Two mice were euthanized, and tumors were collected for ^{1}HR-MAS NMR analysis. The inset of Figure 2a shows images of two tumors: control tumor A (900 mm^3, no

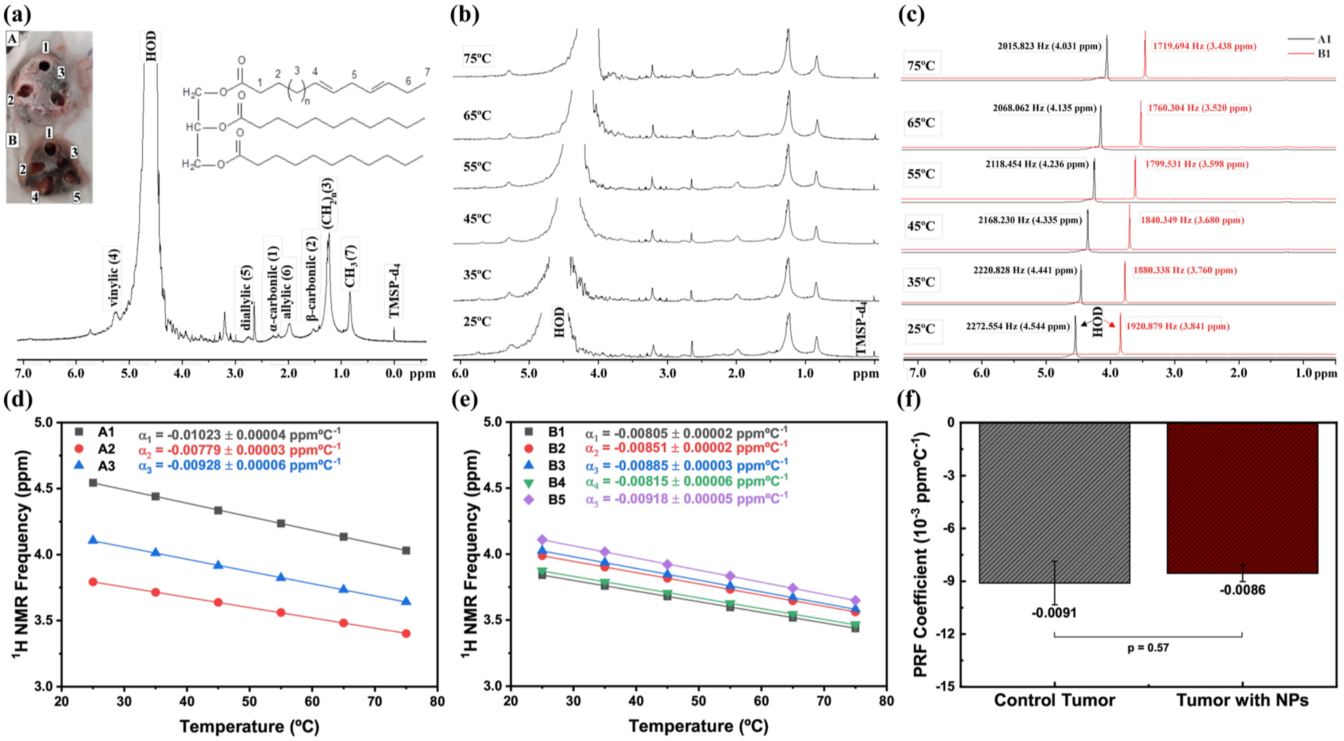

Figure 2. (a) ^{1}HR-MAS NMR spectra of the extracted tumor A (position A1). The inset shows images of tumor A (without NPs) and tumor B (with NPs) and number each corresponding position. It also shows the triacylglyceride formula, highlighting the hydrogens 1 to 7 signals. (b) ^{1}HR-MAS NMR spectra of the tumor A1 at distinct temperatures. (c) ^{1}HR-MAS NMR spectra of the tumors A1 and B1 at distinct temperatures with a focus on HOD signal. (d) Chemical shift temperature dependence at A1, A2 and A3. (e) Chemical shift temperature dependence at B1, B2, B3, B4 and B5. (f) Mean PRF coefficient values estimated for tumor A and tumor B.

NPs) and NP-injected tumor B (1070 mm^3, with NPs injected for PTT). The holes in the tumors mark the sampling locations used to determine the PRF coefficient (see Supporting Information, Figure S4). Tumor spectroscopy data points are numbered in the images. Although the PRF coefficient is established for many tissues,[56] the impact of magnetic NPs and the specific analysis for the B16F10 model have not yet been explored. ^{1}H HR-MAS NMR spectra were acquired using a Bruker Avance III 500 spectrometer (11.75 T, 500 MHz for ^{1}H) with a 4 mm HR-MAS probe spinning at 5 kHz. The samples were prepared with 0.12% (m/m) DMSO-d_6 and TMSP-d_4; details are in Supporting Information, Table S1. Figure 2a shows the ^{1}HR-MAS NMR spectrum for the control tumor (A1 position), highlighting the signals for triacylglycerides (H1−H7). Figure 2b displays temperature-dependent spectra for A1, where only the HOD signal changes with temperature, confirming the inapplicability of PRF thermometry to fat tissues.[20,57] Figure 2c compares the HOD resonance shifts for control (A1, black) and treated tumors (B1, red), showing temperature-dependent shifts due to changes in the strength of hydrogen bonds in water.[20] The presence of NPs slightly alters the resonance position, likely due to susceptibility effects,[57] but PRF shifts remain observable. Figure 2d,e show the dependence of the temperature of the chemical shift for control and treated tumor samples, respectively, with linear fits describing the data. Figure 2f presents the mean PRF coefficient, with values of −0.0091 ± 0.0012 ppm·°C^{-1} for the control tumor and −0.0086 ± 0.0005 ppm·°C^{-1} for the tumor treated with PTT. These values align with those reported in the literature for similar tissues,[56] indicating that low concentrations of NP minimally affect susceptibility effects, and resonance remains dominated by the linear temperature dependence of chemical shift. The effect of higher NP concentrations on the PRF coefficient was evaluated using a pork loin sample. As shown in Figure S5 (Supporting Information), a linear temperature dependence was still observed within the investigated range. The coefficient exhibited a slight variation with increasing NP concentration, but this difference was not statistically significant (p = 0.125). For example, a value of −0.0098 ± 0.0002 ppm·°C^{-1} was obtained for the control sample, which changed to −0.0107 ± 0.0003 ppm·°C^{-1} at 10 mg·mL^{-1}.

3.5. Boundary Determination and Image Artifacts: The Effect of Magnetic NPs in GRE Pulses.

Magnetic materials are known to promote image artifacts that might limit their application. Interestingly, we could not find studies that detail and quantify this issue. So, we designed an experiment to determine the effect for our magnetic NP. Figure 3a shows the experimental design, in which a glass capillary is introduced into a piece of pork loin. The pulse sequences of GRE and Spin echo (SE) of the pork loins are shown in Figure 3c,d, respectively. It is clear that the SE image is not significantly affected by the susceptibility effect under these conditions, while the GRE is highly sensitive. The results suggest that if PTT treatment planning is necessary, the NP distribution is better simulated using SE images for this particular NP. The GRE artifact might arise from NP aggregates that promote high magnetic field inhomogeneities that change the effective transverse relaxation time (T_2*). Since the GRE pulse is the one used for PRF, it can be concluded that the dark regions in the image of the pork loin using 1 mg·mL^{-1} have a larger volume than the real NP distribution. Figure 3b shows the

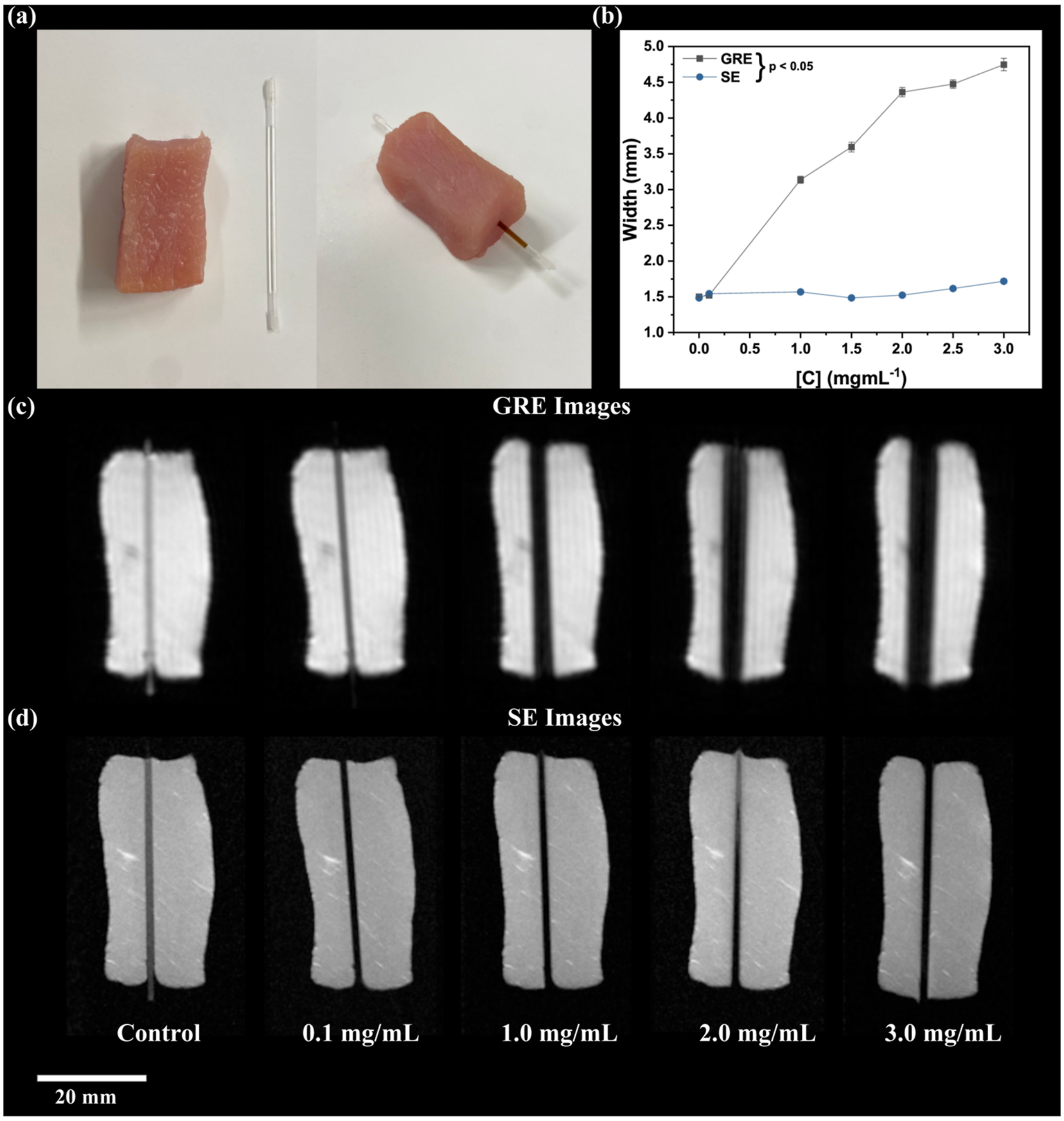

Figure 3. (a) Pork loin pieces with distinct capillaries containing water (control) and the magnetic NPs. (b) Width of the capillary estimated using the spin echo (SE) and gradient recalled echo (GRE) sequences for distinct NP concentration. (c) GRE and (d) SE magnetic resonance images for the capillary inserted pork loin filled with water (control) and different concentrations of NPs.

width estimated in both the SE and GRE images as functions of NP concentration. A statistically significant increase in width was observed in the GRE images (p = 0.031), whereas the SE images remained mostly stable. We found a width increase of around 1.5 mm for the sample of 1 mg·mL^{-1}, indicating a distortion in the image of 0.75 mm for each direction for the GRE case. This effect is certainly a limitation on the use of this particular magnetic NP since it enhances the boundary region containing NPs. However, in the following, we discuss new NP designs that might minimize the effect. The objective of the study is to demonstrate the viability of monitoring the thermal dose in the NP regions using the MRI-PRF method, while it can still be pursued with the knowledge that in the cases reported here the real boundaries are distinct.

3.6. Monitoring Ex Vivo PTT with PRF Thermometry.

The PTT studies were performed in two different experimental configurations for the ablation study: one using the glass capillary design and the other directly injecting NPs into the tissue (see Supporting Information, Figure S6). In both cases, magnetic NPs at 1 mg·mL^{-1} were used. The NP concentration was chosen to generate enough heat during PTT. Figure 4a,b show the experimental setup, including a closer look with the RF coil, the pork loin, the capillary and the fiber optic system used for PTT. Figure 4c shows the GRE MRI images of the control (water) and magnetic NP samples, and the ROIs selected to monitor temperature. As discussed above, the width is distorted due to the susceptibility effect. Figure 4e,f show the PRF MRI thermometry maps at different irradiation times for both samples at 2.5 W·cm^{-2} and 1.0 W·cm^{-2}, respectively. It is clear from the 2D MRI temperature variation maps that the NPs considerably enhance the heat distribution within the tissue during PTT. The control samples only show considerable heat for the high power case close to the laser irradiation region, while the NP-mediated PTT allows heat distribution at deeper conditions, as expected. Figure 4d shows the mean temperature profiles within ROIs for both cases, control and NP, confirming NP-mediated heat generation. The results show statistical difference between the groups. A similar conclusion is obtained for the case where 100 μL of magnetic NPs at 1 mg·mL^{-1} are injected directly into the pork loin and

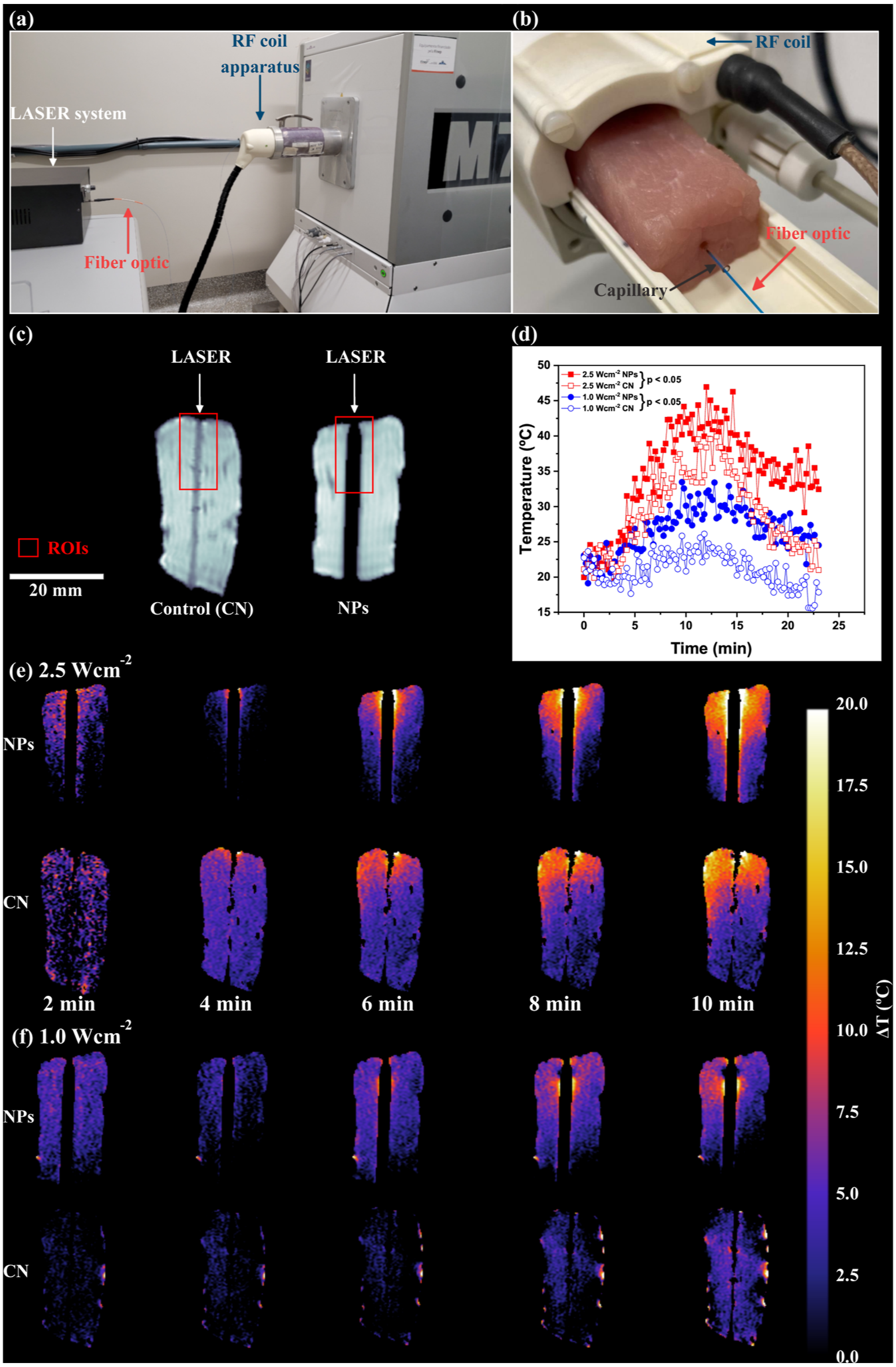

Figure 4. (a) Image of the laser system, fiber optic, RF coil apparatus, and MRI equipment used for PRF thermometry. (b) Close-up view of the RF coil, pork loin, fiber optic, and capillary tube. (c) Reconstructed GRE MRI images of a pork loin with the capillary inserted; on the right, the capillary is filled with 50 μL of water (control—CN), and on the left, it is filled with 50 μg of $MnFe_2O_4$ NPs. Two ROIs and the fiber optic laser positions are highlighted. (d) Temperature profile during the PTT trial for different laser powers (2.5 W·cm^{-2} and 1.0 W·cm^{-2}). (e) 2D temperature variation maps obtained via MRI-PRF thermometry at different times during NP-mediated PTT and water-mediated PTT, both at 2.5 W·cm^{-2}. (f) 2D temperature variation maps at 1.0 W·cm^{-2}.

irradiated at 2.5 W·cm^{-2} (see Supporting Information, Figure S6, for details). Figure S6c shows that the NPs are distributed in a complex arrangement from the injection site. The contrast of T_2 is clear, as well as the distortion effect. Three ROIs were evaluated, one of them close to a temperature probe. The MRI temperature maps are shown at different irradiation times. As

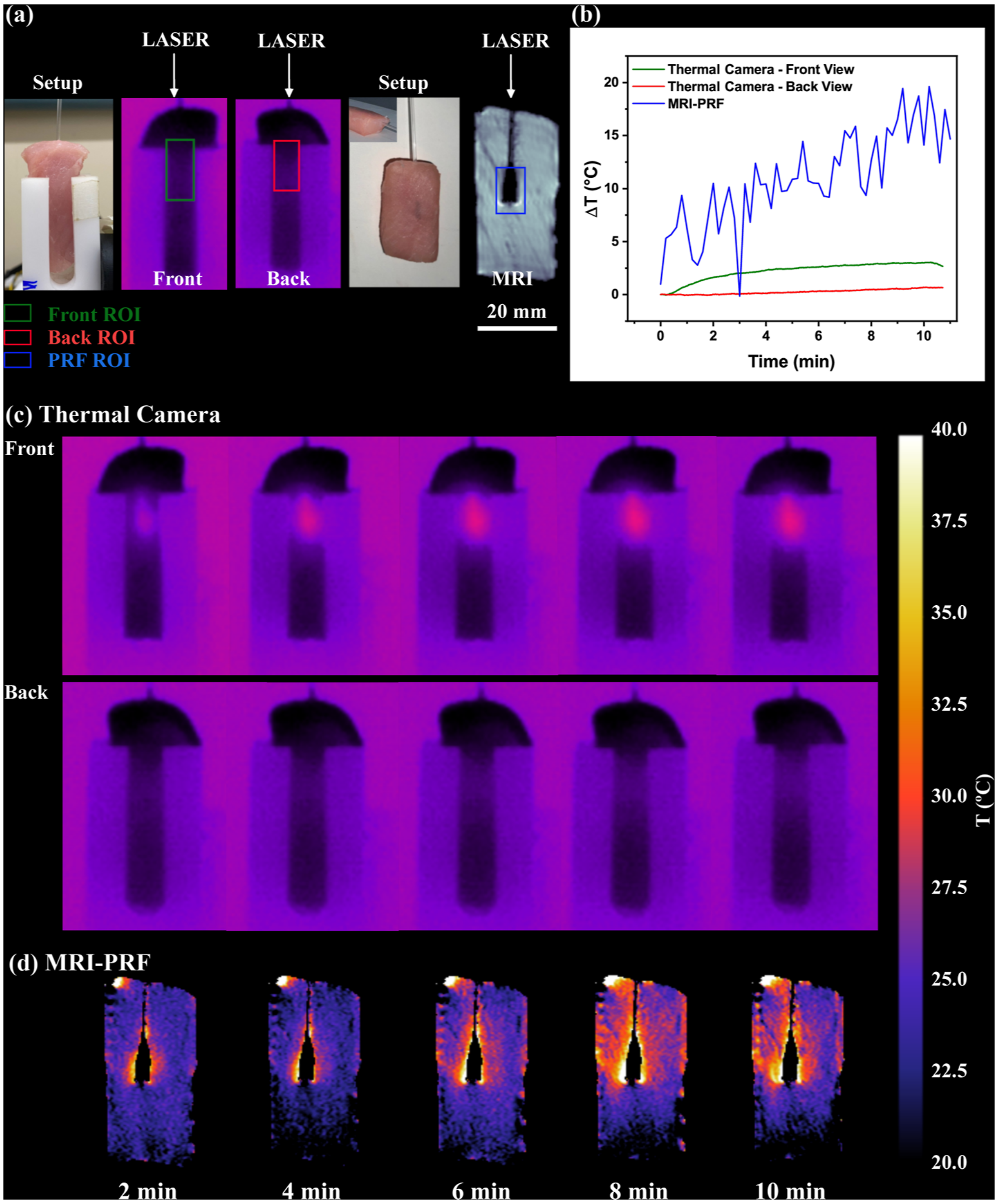

Figure 5. (a) From left to right: setup for the thermal camera study containing a pork loin and sample holder; thermal camera images of the front and back of the setup; setup for the MRI-PRF study with an inset showing the placement of the capillary tube; and reconstructed GRE MRI image of the pork loin with the inserted capillary filled with 10 μL of $MnFe_2O_4$ NPs at 10 mg·mL^{-1}. ROIs and fiber optic laser positions are highlighted. (b) Temperature variation during the studies for a laser fluence of 1.25 W·cm^{-2}. (c) 2D images obtained from the thermal camera study at different times during NP-mediated PTT. (d) 2D temperature variation maps obtained from MRI-PRF thermometry at different times during NP-mediated PTT.

before, heat generation is monitored at the boundary of the NPs, including in deeper regions. In addition, we observe an agreement between measurements in Figure S6b of the ROI close to the temperature probe that validates the methodology. In summary, both studies demonstrate that the boundaries of the NP injection can be monitored using the PRF method.

In addition, we performed a comparison between thermal camera and MRI-PRF thermometry. Figure 5a shows a pork loin with a capillary inserted near one surface to illustrate the limitations of thermal camera thermometry. For the thermal camera study, conducted under the same experimental conditions, the pork sample was placed in a sample holder. In this case, the capillary tube was inserted halfway into the pork loin. Figure 5a also presents the initial images of the back view (far end) and front view (near end) of the pork loin, along with the GRE image used for the PRF thermometry study. All studies—thermal camera (front view), thermal camera (back view), and MRI-PRF—were performed with the capillary tube filled with 10 μL of NP fluid at 10 mg·mL^{-1} and irradiated at 1.25 W·cm^{-2} for 10 min. Temperature maps are shown in Figure 5c,d. The temperature variation graph in Figure 5b shows that the MRI-PRF study detected higher temperature variations (~15 °C), as it measured directly within the capillary tube slice, whereas both thermal camera studies showed significantly lower variations. In the front-view study, where the capillary tube was closer to the surface, temperature change ~3 °C were observed, while the back-view study showed no significant variation. These results clearly

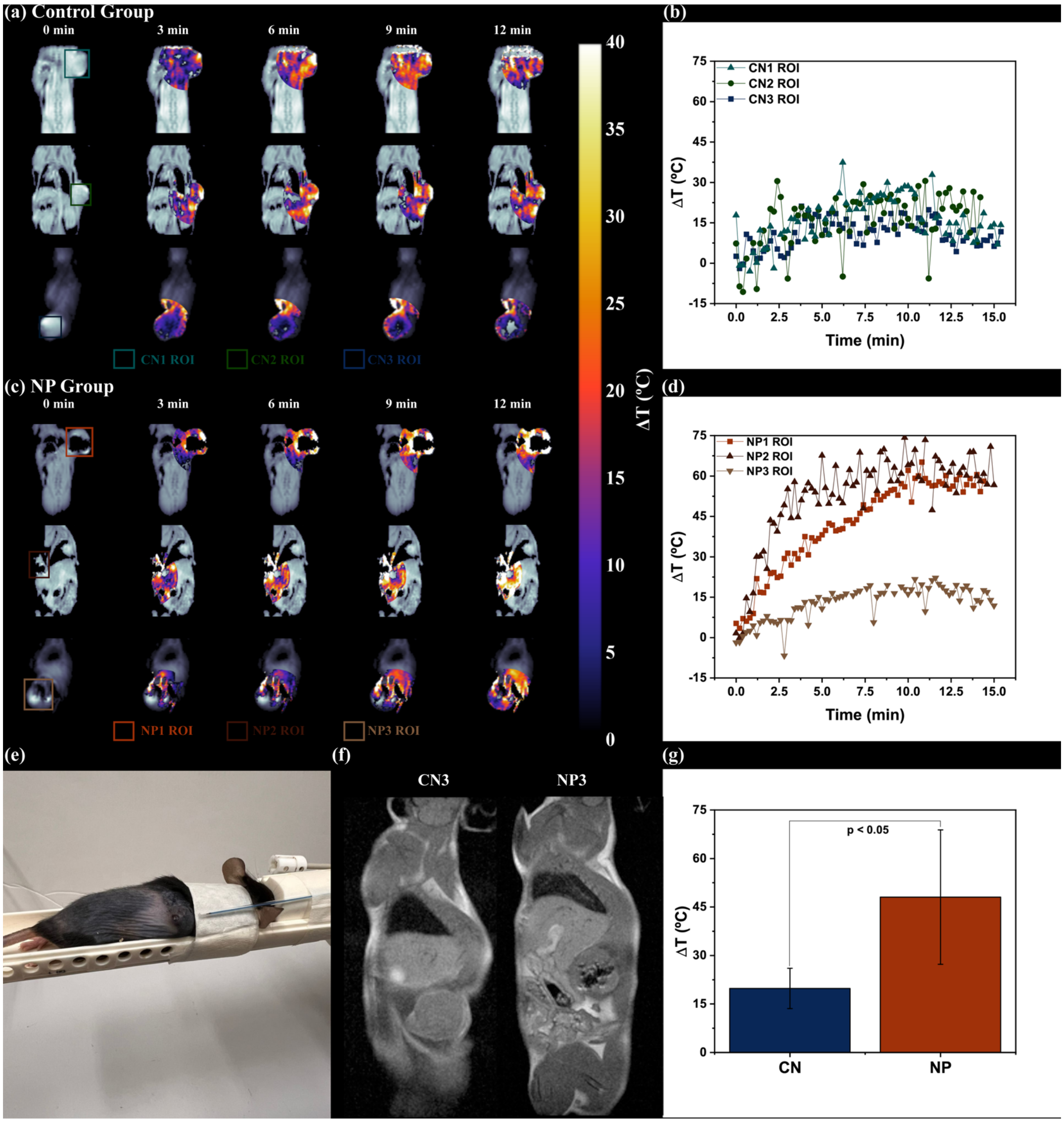

Figure 6. (a) Reconstructed GRE MRI image (at 0 min) merged with 2D temperature maps during laser irradiation for the control group animals. (b) Temperature variation for control group animals. (c) Reconstructed GRE MRI image (at 0 min) merged with 2D temperature maps during laser irradiation for the NP-injected group animals. (d) Temperature variation for NP-injected group animals. (e) Animal position on RF coil. (f) Sagittal T_1W images of one control and one NP-injected animal. (g) Mean temperature increase for the two groups.

demonstrate that MRI-PRF thermometry is more suitable for monitoring temperature in deep-seated tissues, while the thermal camera only detects surface temperature variations.

3.7. MRI-PRF Thermometry during In Vivo NP-Mediated PTT. The control and NP groups, each consisting of three mice, were analyzed in the in vivo study. Figure 6a shows the reconstructed GRE images for each animal in the control group before PTT (0 min) and their respective regions of interest (ROIs) used for temperature monitoring. It also presents temperature maps in the tumor region merged with the baseline image at 3 min intervals. The temperature increases observed for CN1, CN2, and CN3 are shown in Figure 6b. Figure 6c displays the images obtained for the NP group, where the T_2 contrast effect of the NPs is visible in the tumors. All animals in this group exhibited a temperature increase, with NP1 and NP2 showing pronounced heating, as evidenced by both the temperature maps and the temperature variation plots in Figure 6d. The third NP-injected animal (NP3) showed lower heating, which could be attributed to a possible misalignment in the irradiation region, as suggested by the heating map distribution. Additionally, higher blood perfusion in the ROI of this animal may have contributed to the reduced temperature rise. The differences observed among NP1−NP3 likely reflect variations in both perfusion and NP distribution within the tumors. This effect has been previously reported in another PTT study by our group, in which heat delivery was monitored using a thermal camera.[32] A comparative video of the temperature maps for CN1 and NP1 is provided in Supporting Information, Video S1. Figure 6e shows the positioning of one of the animals in the holding system and the optical fiber laser access to the tumor. Figure 6f presents sagittal T_1W SE images of CN3 and NP3, where tumor visualization and NP distribution can be better observed in the latter. Figure 6g shows the mean temperature increase after 10 min of laser irradiation for both groups. The mean temperature variation during PTT was 19.8 ± 6.2 °C for the control group and 48.1 ± 20.8 °C for the NP-injected group.

The difference was statistically significant ($p = 0.0186$), confirming NP-mediated heat generation.

3.8. Histopathological Analysis Revealed Higher Efficiency in the NP-Treated Group after PTT.

Histopathological analysis revealed that tumors from both the control and NP-treated animals exhibited typical features of apoptosis/necrosis (Figure 7a,b). However, NP-treated tumors showed greater intensity and extent of tissue damage, with granular parenchyma, amorphous, and eosinophilic, characterized by extensive and confluent areas of apoptotic/necrotic cells. Cellular analysis of NP-treated tumors revealed large regions of cells with pyknotic nuclei, heterochromatic bodies in the cytoplasm (karyorrhexis), and apoptotic bodies (karyolysis) (Figure 7b). This level of damage was not observed in control tumors, which maintained greater tissue and cellular integrity (Figure 7a). These results correlate with the higher thermal dose delivered to the NP-treated group. No iron was detected in the tumors of control animals (Figure 7c), whereas NP-treated tumors exhibited considerable iron (Fe) accumulation, as indicated by Perls' staining, with a heterogeneous distribution throughout the tissue (Figure 7d). This confirms that the NPs remained at the injection site after intratumoral administration.

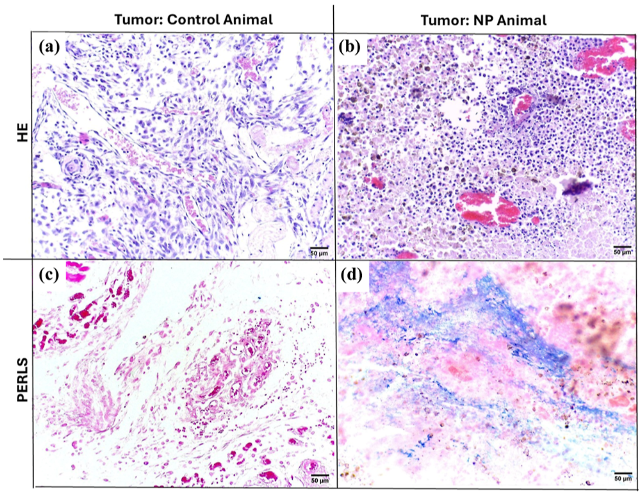

Figure 7. Histopathological analysis. Hematoxylin and eosin (HE) and Perls (iron identification) staining in tumors. (a) Tumor control (HE)—more organized parenchyma and few aspects related to apoptosis/necrosis, showing lower lesion intensity. (b) Tumor control with NP (HE) shows clear evidence of necrosis/apoptosis. (c) Tumor control (Perls staining)—iron-free. (d) Tumor control with NP (Perls staining)—there is intense Perls iron content in the tumor with NP (blue spots). Scale bars are equivalent to 50 μm at 20× magnification.

The tissues of both animal groups (heart, liver, kidney, spleen, lung, and brain) showed no changes in parenchyma and no signs of cellular infiltration, hyperemia, necrosis, or apoptosis, as shown in Supporting Information, Figure S7a. No NPs were detected in the heart, kidneys, lungs, liver, or brain of NP-inoculated animals (Supporting Information, Figure S7b). However, a very small amount of iron was detected in the spleen, which could be related to the presence of endogenous iron resulting from the recycling of aged red blood cells. We cannot, however, exclude the possibility of NP uptake by intratumoral macrophages followed by trafficking to the spleen. Interestingly, no evidence of this phenomenon was observed in the liver. These results suggest that the NPs were largely restricted to the tumor after intratumoral administration.

3.9. Mn-Ferrite Nanoparticles for Intratumoral PTT Are Active within a Safe Concentration Range.

NPs can biodegrade by releasing metal ions due to the acidic environment inside cells (endosomes/lysosomes) or the tumor microenvironment, and PTT can enhance this effect.[58] The release of Fe and Mn can promote ferroptosis through Fenton-like reactions or modulate macrophage polarization from the M2 to the M1 state.[29,59] Indeed, Mn has been recognized as critical for metalloimmunotherapy,[30,60] being associated with enhanced natural killer cell activity in mice, release of inflammatory cytokines, amplification of the STING signaling pathway, and induction of robust antitumor T cell responses.[30,60] All of these effects are beneficial for tumor treatment. However, concerns mainly arise for Mn ions due to a well-known neurological disorder called manganism, which can occur in workers exposed to manganese through inhalation in occupations such as mining, welding, and battery manufacturing. Neurological damage is expected if Mn levels in the brain exceed a threshold. According to a recent study, the median lethal dose of $MnCl_2$ in mice is 1715 mg/kg,[60] whereas neurodegenerative disorders may occur at concentrations above 38−175 mg/kg.[61] In our study, the estimated intratumoral dose was 4.5 mg of $MnFe_2O_4$ NPs/kg. Mn ions may be released locally from the NP surfaces at much lower levels. Mn is an essential cofactor for several enzymes,[61] making it unlikely that significant amounts of Mn ions would enter the bloodstream and accumulate in the brain at harmful doses. In Supporting Information, Figure S8 shows that the tumor of an NP-treated animal exhibits significant T_2 contrast differences compared with a control animal, while other organs show no changes. Brain MRI images further confirm the absence of Mn accumulation, at least up to 2 weeks after intratumoral PTT. Previous studies using the same type of NP administered intravenously indicate that NPs accumulate in the liver, with most being eliminated via the hepatic route.[49] Smaller NPs (less than 5 nm) released into the bloodstream are expected to be cleared by the kidneys and should not cross the blood−brain barrier. For humans, a similar NP concentration is expected to generate the reported thermal dose. Notably, Western diets provide up to 10 mg/day of Mn, which is far higher than the amount administered intratumorally for PTT.[60]

3.10. Challenges and Opportunities for Magnetic NP-Mediated PTT Using MRI-PRF Thermometry.

The susceptibility effect, in particular the magnetic field inhomogeneities due to the magnetic NP arrangements (single-core or multicore nanostructures), is certainly one of the great challenges in using magnetic NPs for PTT while monitored by MRI-PRF thermometry. The term should depend on the square of the saturation magnetization and the NP volume. Therefore, we expect that, with decreasing particle size, the artifact volume effect will decrease considerably, resulting in better-determined boundaries. Surface effects also decrease the NP saturation magnetization that can influence the phenomena.[52] Core−shell engineering might also play a role, for instance, gold-coated magnetic NPs might reduce the susceptibility effect and enhance PTT performance.[62] Furthermore, there are even reports in the literature that low particle sizes make magnetic NPs T_1 contrast agents,[55] which could allow thermal dose monitoring even where the NP is distributed. The above discussions suggest that there is plenty of room for improvement.

4. CONCLUSION

In summary, we demonstrated that magnetic NPs can be used for MRI-guided PTT despite signal loss in accumulation areas due to relaxation effects, provided the concentration of NP remains low enough to minimize susceptibility effects. A temperature-dependent ^{1}HR-MAS NMR study of B16F10 tumors containing NPs supported this conclusion. Thermal therapy monitoring using the MRI proton resonance frequency shift (PRF) method is feasible at the injection site boundaries. However, susceptibility effects resulted in apparent larger boundaries for this magnetic NP size. Using Mn-doped iron oxide NPs with T_2 contrast properties and high photothermal conversion efficiency, we implemented the PRF method in a preclinical MRI system. Ex vivo validation confirmed the thermometry method, while in vivo experiments showed advantages of nanoparticle-mediated PTT over laser therapy alone, including improved tumor temperature distribution and potential nanoparticle-mediated immunotherapy effects. Given that iron oxide-based NPs have been clinically used for decades, their application in PTT, combined with MRI thermometry for thermal dose monitoring, holds significant potential for clinical translation. We hope that this study inspires further advances in magnetic NPs and the design of NP-mediated thermal immunotherapies.

■ ASSOCIATED CONTENT

Data Availability Statement

Data supporting the findings of this study are available upon reasonable request from the authors.

Supporting Information

The Supporting Information is available free of charge at https://pubs.acs.org/doi/10.1021/acsanm.5c03647.

^{1}H HR-MAS NMR spectroscopy details; signal recovery/decay vs inversion/echo time for ProHance and magnetic NPs; absorbance curve for Mn-ferrite sample; zeta potential data; ^{1}H HR-MAS NMR spectroscopy for tumor samples; ^{1}H HR-MAS NMR spectroscopy for pork loin pieces; PTT study of NP injected into the piece of pork loin; histopathological analysis of noble organs; MRI biodistribution images (PDF)

PTT in vivo MRI-PRF thermometry video (MP4)

■ AUTHOR INFORMATION

Corresponding Author

Andris Figueiroa Bakuzis − *Institute of Physics, Federal University of Goiás, Goiânia, Goiás 74690-900, Brazil; CNanoMed, Nanomedicine Integrated Research Center, Federal University of Goiás, Goiânia, Goiás 74690-631, Brazil;* orcid.org/0000-0003-3366-106X;
Email: bakuzis@ufg.br

Authors

Rafael Freire Krause − *Institute of Physics, Federal University of Goiás, Goiânia, Goiás 74690-900, Brazil*
Maria de Paula Pereira − *Institute of Physics, Federal University of Goiás, Goiânia, Goiás 74690-900, Brazil*
Carlos Eduardo Ribeiro − *Institute of Physics, Federal University of Goiás, Goiânia, Goiás 74690-900, Brazil*
João Victor Ribeiro Rocha − *Institute of Physics, Federal University of Goiás, Goiânia, Goiás 74690-900, Brazil*
Marcus Vinícius-Araújo − *Institute of Physics, Federal University of Goiás, Goiânia, Goiás 74690-900, Brazil;* orcid.org/0000-0002-4519-8407
Lucas Ferreira Martins − *Institute of Chemistry, Federal University of Goiás, Goiânia, Goiás 74690-900, Brazil;* orcid.org/0000-0003-0223-8568
Juracy Leandro Santos Junior − *Institute of Physics, Federal University of Goiás, Goiânia, Goiás 74690-900, Brazil*
Clever Gomes Cardoso − *Institute of Biology, Federal University of Goiás, Goiânia, Goiás 74690-900, Brazil;* orcid.org/0000-0002-9175-7695
Marcilia Viana Pavam − *Farmatec, Laboratory of Pharmaceutical Technology and CNanoMed, Nanomedicine Integrated Research Center, Federal University of Goiás, Goiânia, Goiás 74690-631, Brazil*
Luciano Morais Lião − *Institute of Chemistry, Federal University of Goiás, Goiânia, Goiás 74690-900, Brazil;* orcid.org/0000-0001-9985-2980

Complete contact information is available at:
https://pubs.acs.org/10.1021/acsanm.5c03647

Funding

The Article Processing Charge for the publication of this research was funded by the Coordenacao de Aperfeicoamento de Pessoal de Nivel Superior (CAPES), Brazil (ROR identifier: 00x0ma614).

Notes

The authors declare no competing financial interest.

■ ACKNOWLEDGMENTS

M.V.-A. acknowledges the financial support provided by the Conselho Nacional de Desenvolvimento Científico e Tecnológico—CNPq, grant 380286/2024-6. A.F.B. acknowledges the financial support of the CNPq grants 312458/2021-5 and 405139/2023-3. The authors also thank the LabMic-UFG for access to the Electron Microscopy facilities at UFG, CRTI-UFG for XRD data, FarmaTec for zeta potential data, LabRMN for NMR data, and CNanoMed for AC susceptibility and MRI data.

■ REFERENCES

(1) Yang, Z.; Gao, D.; Zhao, J.; Yang, G.; Guo, M.; Wang, Y.; Ren, X.; Kim, J. S.; Jin, L.; Tian, Z.; Zhang, X. *Nat. Rev. Clin. Oncol.* **2023**, *20*, 116−134.

(2) Hildebrandt, B. *Crit. Rev. Oncol. Hematol.* **2002**, *43*, 33−56.

(3) Rodrigues, H. F.; Capistrano, G.; Bakuzis, A. F. *Int. J. Hyperther.* **2020**, *37*, 76−99.

(4) Rastinehad, A. R.; Anastos, H.; Wajswol, E.; Winoker, J. S.; Sfakianos, J. P.; Doppalapudi, S. K.; Carrick, M. R.; Knauer, C. J.; Taouli, B.; Lewis, S. C.; Tewari, A. K.; Schwartz, J. A.; Canfield, S. E.; George, A. K.; West, J. L.; Halas, N. J. *Proc. Natl. Acad. Sci. U.S.A.* **2019**, *116*, 18590−18596.

(5) Pappone, C.; Vicedomini, G.; Manguso, F.; Saviano, M.; Baldi, M.; Pappone, A.; Ciaccio, C.; Giannelli, L.; Ionescu, B.; Petretta, A.; Vitale, R.; Cuko, A.; Calovic, Z.; Fundaliotis, A.; Moscatiello, M.; Tavazzi, L.; Santinelli, V. *Circulation* **2014**, *130*, 811−819.

(6) Hoppe, C.; Witt, J.-A.; Helmstaedter, C.; Gasser, T.; Vatter, H.; Elger, C. E. *Seizure* **2017**, *48*, 45−52.

(7) Salem, U.; Kumar, V. A.; Madewell, J. E.; Schomer, D. F.; de Almeida Bastos, D. C.; Zinn, P. O.; Weinberg, J. S.; Rao, G.; Prabhu, S. S.; Colen, R. R. *Cancer Imaging* **2019**, *19*, 65.

(8) Deng, T.; Zhang, L.; Li, X.; Zink, J. I.; Wu, H. H. *ACS Nano* **2021**, *15*, 14618−14630.

(9) Bastos, D. C. d. A.; Fuentes, D. T.; Traylor, J.; Weinberg, J.; Kumar, V. A.; Stafford, J.; Li, J.; Rao, G.; Prabhu, S. S. *Int. J. Hyperther.* **2020**, *37*, 53−60.

(10) Ahmed, M.; Brace, C. L.; Lee, F. T.; Goldberg, S. N. *Radiology* **2011**, *258*, 351−369.

(11) Vinícius-Araújo, M.; Shrivastava, N.; Sousa-Junior, A. A.; Mendanha, S. A.; Santana, R. C. D.; Bakuzis, A. F. *ACS Appl. Nano Mater.* **2021**, *4*, 2190−2210.

(12) Borys, N.; Dewhirst, M. W. *Adv. Drug Delivery Rev.* **2021**, *178*, 113985.

(13) Cintra, E. R.; Hayasaki, T. G.; Sousa-Junior, A. A.; Silva, A. C. G.; Valadares, M. C.; Bakuzis, A. F.; Mendanha, S. A.; Lima, E. M. *Front. Pharmacol* **2022**, *13*, 854430.

(14) Rodrigues, H. F.; Capistrano, G.; Bakuzis, A. F. *Int. J. Hyperther.* **2020**, *37*, 76−99.

(15) Vaz, J. D. B.; Castro, S. d. M.; Pavam, M. V.; Lima, E. M.; Mendanha, S. A.; Bakuzis, A. F. *Adv. Mater. Technol.* **2024**, *10*, 2401598.

(16) Kokuryo, D.; Kumamoto, E.; Kuroda, K. *Adv. Drug Delivery Rev.* **2020**, *163*, 19−39.

(17) Rieke, V.; Butts Pauly, K. *J. Magn. Reson. Imaging* **2008**, *27*, 376−390.

(18) Chen, Y.; Gnyawali, S. C.; Wu, F.; Liu, H.; Tesiram, Y. A.; Abbott, A.; Towner, R. A.; Chen, W. R. *J. Biomed. Opt.* **2008**, *13*, 044033.

(19) Yuan, J.; Mei, C.-S.; Panych, L. P.; McDannold, N. J.; Madore, B. *Quant. Imaging Med. Surg.* **2012**, *2*, 21−32.

(20) Odéen, H.; Parker, D. L. *Prog. Nucl. Magn. Reson. Spectrosc.* **2019**, *110*, 34−61.

(21) Blackwell, J.; Kraśny, M. J.; O'Brien, A.; Ashkan, K.; Galligan, J.; Destrade, M.; Colgan, N. *J. Magn. Reson. Imaging* **2022**, *55*, 389−403.

(22) Li, X.; Lovell, J. F.; Yoon, J.; Chen, X. *Nat. Rev. Clin. Oncol.* **2020**, *17*, 657−674.

(23) Hirsch, L. R.; Stafford, R. J.; Bankson, J.; Sershen, S. R.; Rivera, B.; Price, R.; Hazle, J. D.; Halas, N. J.; West, J. L. *Proc. Natl. Acad. Sci. U.S.A.* **2003**, *100*, 13549−13554.

(24) Kadria-Vili, Y.; Neumann, O.; Zhao, Y.; Nordlander, P.; Martinez, G. V.; Bankson, J. A.; Halas, N. J. *Proc. Natl. Acad. Sci. U.S.A.* **2022**, *119*, No. e2123527119.

(25) Meng, X.; Zhang, B.; Yi, Y.; Cheng, H.; Wang, B.; Liu, Y.; Gong, T.; Yang, W.; Yao, Y.; Wang, H.; Bu, W. *Nano Lett.* **2020**, *20*, 2522−2529.

(26) Pan, D.; Caruthers, S. D.; Senpan, A.; Schmieder, A. H.; Wickline, S. A.; Lanza, G. M. *Wiley Interdiscip. Rev. Nanomed. Nanobiotechnol.* **2011**, *3*, 162−173.

(27) Anselmo, A. C.; Mitragotri, S. *Bioeng. Transl. Med.* **2016**, *1*, 10−29.

(28) Anselmo, A. C.; Mitragotri, S. *Bioeng. Transl. Med.* **2021**, *6*, No. e10246.

(29) Zanganeh, S.; Hutter, G.; Spitler, R.; Lenkov, O.; Mahmoudi, M.; Shaw, A.; Pajarinen, J. S.; Nejadnik, H.; Goodman, S.; Moseley, M.; Coussens, L. M.; Daldrup-Link, H. E. *Nat. Nanotechnol.* **2016**, *11*, 986−994.

(30) Li, J.; Ren, H.; Zhang, Y. *Coord. Chem. Rev.* **2022**, *455*, 214345.

(31) Fang, R. H.; Gao, W.; Zhang, L. *Nat. Rev. Clin. Oncol.* **2023**, *20*, 33−48.

(32) Sousa-Junior, A. A.; Mello-Andrade, F.; Rocha, J. V. R.; Hayasaki, T. G.; de Curcio, J. S.; Silva, L. d. C.; de Santana, R. C.; Martins Lima, E.; Cardoso, C. G.; Silveira-Lacerda, E. d. P.; Mendanha, S. A.; Bakuzis, A. F. *Pharmaceutics* **2023**, *15*, 943.

(33) de Moraes, E. C.; Siqueira Furtuoso Rodrigues, M. M.; de Menezes, R. C.; Vinícius-Araújo, M.; Valadares, M. C.; Bakuzis, A. F. *ACS Biomater. Sci. Eng.* **2025**, *11*, 1084−1095.

(34) Sweeney, E. E.; Cano-Mejia, J.; Fernandes, R. *Small* **2018**, *14*, 1800678.

(35) Ito, A.; Honda, H.; Kobayashi, T. *Cancer Immunol. Immunother.* **2006**, *55*, 320−328.

(36) Toraya-Brown, S.; Sheen, M. R.; Zhang, P.; Chen, L.; Baird, J. R.; Demidenko, E.; Turk, M. J.; Hoopes, P. J.; Conejo-Garcia, J. R.; Fiering, S. *Nanomed. Nanotechnol. Biol. Med.* **2014**, *10*, 1273−1285.

(37) Neto, L. M. M.; Zufelato, N.; de Sousa-Júnior, A. A.; Trentini, M. M.; da Costa, A. C.; Bakuzis, A. F.; Kipnis, A.; Junqueira-Kipnis, A. P. *Hum. Vaccines Immunother.* **2018**, *14*, 2786−2801.

(38) Capistrano, G.; Rodrigues, H. F.; Zufelato, N.; Gonçalves, C.; Cardoso, C. G.; Silveira-Lacerda, E. P.; Bakuzis, A. F. *Int. J. Hyperther.* **2020**, *37*, 120−140.

(39) Rocha, J. V. R.; Krause, R. F.; Ribeiro, C. E.; Oliveira, N. C. d. A.; Ribeiro de Sousa, L.; Leandro Santos, J. J.; Castro, S. d. M.; Valadares, M. C.; Cunha Xavier Pinto, M.; Pavam, M. V.; Lima, E. M.; Antônio Mendanha, S.; Bakuzis, A. F. *ACS Appl. Mater. Interfaces* **2025**, *17*, 13094−13110.

(40) Quini, C. C.; Próspero, A. G.; Calabresi, M. F.; Moretto, G. M.; Zufelato, N.; Krishnan, S.; Pina, D. R.; Oliveira, R. B.; Baffa, O.; Bakuzis, A. F. *Nanomed. Nanotechnol. Biol. Med.* **2017**, *13*, 1519−1529.

(41) Kalaiselvan, C. R.; Laha, S. S.; Somvanshi, S. B.; Tabish, T. A.; Thorat, N. D.; Sahu, N. K. *Coord. Chem. Rev.* **2022**, *473*, 214809.

(42) Yang, K.; Yu, G.; Tian, R.; Zhou, Z.; Deng, H.; Li, L.; Yang, Z.; Zhang, G.; Liu, D.; Wei, J.; et al. Oxygen-Evolving Manganese Ferrite Nanovesicles for Hypoxia-Responsive Drug Delivery and Enhanced Cancer Chemoimmunotherapy. *Adv. Funct. Mater.* **2021**, *31*, 2008078.

(43) Lee, J.-H.; Huh, Y.-M.; Jun, Y.-w.; Seo, J.-w.; Jang, J.-t.; Song, H.-T.; Kim, S.; Cho, E.-J.; Yoon, H.-G.; Suh, J.-S.; et al. Artificially engineered magnetic nanoparticles for ultra-sensitive molecular imaging. *Nat. Med.* **2007**, *13*, 95−99.

(44) Ribeiro, C. E.; Vinícius-Araújo, M.; Bakuzis, A. F. *ACS Appl. Nano Mater.* **2025**, *8*, 7061−7072.

(45) Capistrano, G.; Sousa-Junior, A. A.; Silva, R. A.; Mello-Andrade, F.; Cintra, E. R.; Santos, S.; Nunes, A. D.; Lima, R. M.; Zufelato, N.; Oliveira, A. S.; et al. IR-780-Albumin-Based Nanocarriers Promote Tumor Regression Not Only from Phototherapy but Also by a Nonirradiation Mechanism. *ACS Biomater. Sci. Eng.* **2020**, *6*, 4523−4538.

(46) Zhou, B.; Wu, Q.; Wang, M.; Hoover, A.; Wang, X.; Zhou, F.; Towner, R. A.; Smith, N.; Saunders, D.; Song, J.; et al. Immunologically modified MnFe2O4 nanoparticles to synergize photothermal therapy and immunotherapy for cancer treatment. *Chem. Eng. J.* **2020**, *396*, 125239.

(47) Sun, R.; Ge, Y.; Liu, H.; He, P.; Song, W.; Zhang, X. *ACS Appl. Bio Mater.* **2021**, *4*, 701−710.

(48) Prospero, A. G.; Fidelis-de Oliveira, P.; Soares, G. A.; Miranda, M. F.; Pinto, L. A.; Dos Santos, D. C.; Silva, V. d. S.; Zufelato, N.; Bakuzis, A. F.; Miranda, J. R. *Nanomedicine* **2020**, *15*, 511−525.

(49) Soares, G. A.; Faria, J. V.; Pinto, L. A.; Prospero, A. G.; Pereira, G. M.; Stoppa, E. G.; Buranello, L. P.; Bakuzis, A. F.; Baffa, O.; Miranda, J. R. *Materials* **2022**, *15*, 2121.

(50) Roper, D. K.; Ahn, W.; Hoepfner, M. *J. Phys. Chem. C* **2007**, *111*, 3636−3641.

(51) Paściak, A.; Marin, R.; Abiven, L.; Pilch-Wróbel, A.; Misiak, M.; Xu, W.; Prorok, K.; Bezkrovnyi, O.; Marciniak, Ł.; Chanéac, C. *ACS Appl. Mater. Interfaces* **2022**, *14*, 33555−33566.

(52) Tang, Z.; Sorensen, C.; Klabunde, K.; Hadjipanayis, G. *Phys. Rev. Lett.* **1991**, *67*, 3602.

(53) Verde, E. L.; Landi, G. T.; Carrião, M.; Drummond, A. L.; Gomes, J.; Vieira, E.; Sousa, M.; Bakuzis, A. F. *AIP Adv.* **2012**, *2*, 032120.

(54) Peters, J. A. *Prog. Nucl. Magn. Reson. Spectrosc.* **2020**, *120−121*, 72−94.

(55) Pernia Leal, M.; Rivera-Fernández, S.; Franco, J. M.; Pozo, D.; de la Fuente, J. M.; García-Martín, M. L. *Nanoscale* **2015**, *7*, 2050−2059.

(56) McDannold, N. *Int. J. Hyperther.* **2005**, *21*, 533−546.

(57) Poorter, J. D. *Magn. Reson. Med.* **1995**, *34*, 359−367.

(58) Fromain, A.; Perez, J. E.; Van de Walle, A.; Lalatonne, Y.; Wilhelm, C. *Nat. Commun.* **2023**, *14*, 4637.

(59) Cheng, J.; Zhu, Y.; Xing, X.; Xiao, J.; Chen, H.; Wang, D.; Zhang, Y.; Zhang, G.; Wu, Z.; Liu, Y. *Theranostics* **2021**, *11*, 5418−5429.

(60) Sun, X.; Zhang, Y.; Li, J.; Park, K. S.; Han, K.; Zhou, X.; Xu, Y.; Nam, J.; Xu, J.; Shi, X.; Wei, L.; Lei, Y. L.; Moon, J. J. *Nat. Nanotechnol.* **2021**, *16*, 1260−1270.

(61) Silva, A. C.; Bock, N. A. *Schizophr. Bull.* **2007**, *34*, 595−604.

(62) Hu, Y.; Wang, R.; Wang, S.; Ding, L.; Li, J.; Luo, Y.; Wang, X.; Shen, M.; Shi, X. *Sci. Rep.* **2016**, *6*, 28325.